

Self-Powered Portable Nanowire Array Gas Sensor for Dynamic NO₂ monitoring at room temperature

Shiyu Wei, Zhe Li, Krishnan Murugappan, Ziyuan Li, Fanlu Zhang, Aswani Gopakumar Saraswathyvilasam, Mykhaylo Lysevych, Hark Hoe Tan, Chennupati Jagadish, Antonio Tricoli*, and Lan Fu**

S. Wei, F. Zhang, Dr. Z. Y. Li, Prof. H. H. Tan, Prof. C. Jagadish, Prof. L. Fu

Australian Research Council Centre of Excellence for Transformative Meta-Optical Systems, Department of Electronic Materials Engineering, Research School of Physics, The Australian National University, Canberra, ACT 2601, Australia

Dr. Z. Li and A. G. Saraswathyvilasam

Department of Electronic Materials Engineering, Research School of Physics, The Australian National University, Canberra, ACT 2601, Australia

Dr. M. Lysevych

Australian National Fabrication Facility, The Australian National University, Canberra, ACT 2601, Australia

Dr. K. Murugappan

This is the author manuscript accepted for publication and has undergone full peer review but has not been through the copyediting, typesetting, pagination and proofreading process, which may lead to differences between this version and the [Version of Record](#). Please cite this article as [doi: 10.1002/adma.202207199](https://doi.org/10.1002/adma.202207199).

This article is protected by copyright. All rights reserved.

Nanotechnology Research Laboratory, Research School of Chemistry, College of Science, The Australian National University, Canberra, ACT 2601, Australia

Commonwealth Scientific and Industrial Research Organisation (CSIRO), Mineral Resources, Private Bag 10, Clayton South, Victoria, 3169, Australia

Prof. A. Tricoli

Nanotechnology Research Laboratory, Faculty of Engineering, The University of Sydney, Camperdown 2006, Australia

Nanotechnology Research Laboratory, Research School of Chemistry, College of Science, The Australian National University, Canberra, ACT 2601, Australia

E-mail: zhe.li@anu.edu.au; antonio.tricoli@anu.edu.au; lan.fu@anu.edu.au

Keywords: Self-powered, p-n homojunction, InP nanowire, gas sensor

Abstract

The fast development of the Internet of Things (IoT) has driven an increasing consumer demand of self-powered gas sensors for real-time data collection and autonomous responses in industries such as environmental monitoring, workplace safety, smart cities, and personal healthcare. Despite intensive research and rapid progress in the field, most reported self-powered devices, specifically NO₂ sensors for air pollution monitoring, have limited sensitivity, selectivity, and scalability. Here, a novel photovoltaic self-powered NO₂ sensor is demonstrated based on axial p-i-n homojunction InP nanowire (NW) arrays, that overcome these limitations. The optimized innovative InP NW array device was designed by numerical simulation for insights into sensing mechanisms and performance enhancement. Without a power source, this InP NW sensor achieves an 84% sensing response to 1

This article is protected by copyright. All rights reserved.

ppm NO₂ and records a limit of detection down to the sub-ppb level, with little dependence on the incident light intensity, even under <5% of 1 sun illumination. Based on this great environmental fidelity, the sensor was integrated onto a commercial microchip interface to evaluate its performance in the context of dynamic environmental monitoring of motor vehicle exhaust. Our results show that compound semiconductor nanowires can form promising self-powered sensing platforms suitable for future mega-scale IoT systems.

1. Introduction

The large-scale implementation of Internet of Things (IoT) technology over the recent decade has increased consumer demand for reliable and accurate gas sensor networks for real-time data collection and autonomous response in applications such as air pollution monitoring, industrial chemical hazard detection, smart cities and personal healthcare.^[1-2] Given the immense number of sensors required to feed into such a network, there is an urgent need to obtain sensors with characteristics such as being micro- or nano-sized, ever superior sensitivity and detectivity, shorter response times, and critically require orders of magnitude less power consumption than current commercial devices.^[3-4] Conventional battery-powered sensors not only require continuous power supply during operation but are difficult to miniaturize, limiting their use in highly integrated systems.^[5-6] Self-powered sensing systems are one of the most promising solutions to overcome both the power supply issue and achieve miniaturization.^[7-9] Such systems can harvest energy from the environment such as sunlight, body motion, and heat, to realize zero-power consumption.^[6, 10] Among these different types of self-powered gas sensors, photovoltaic (PV) effect based sensors are being explored, as PV effect and gas sensing function can be achieved simultaneously within the same junction or semiconductor active layer.^[11] This simplified structure is low-cost and has a simpler fabrication process, which are desirable characteristics for their possible integration into next generation IoT systems.^[12]

This article is protected by copyright. All rights reserved.

Over the past decade, self-powered PV gas sensors have been demonstrated by forming p-n or Schottky junctions based on a variety of bulk or low-dimensional materials, including 2D materials (e.g. graphene, WS₂, and WSe₂),^[13-14] metal oxide,^[15] perovskite,^[16] carbon nanotube,^[17] and hyper-doped Si^[18-19]. However, most of the reported self-powered gas sensors show issues such as limited sensitivity and selectivity at room temperature,^[20] signal drifts and lack of stability over time,^[21-22] as well as challenges in integration with complementary metal-oxide-semiconductor (CMOS) based technology.^[16] Also, in these sensors, the junction regions are often buried within the devices and do not interact with gas molecules due to the limitation of device architectures.^[11]

III-V compound semiconductors are the key materials for record-efficiency single- and multi-junction solar cells^[23] due to their direct and tunable bandgap, superior optical and electronic properties. III-V compound semiconductor nanowires (NWs) have also been widely investigated for solar cell applications.^[24, 25] Compared with other III-V NWs, InP NWs show lower surface recombination velocity and higher carrier mobility, which is ideal for solar cell applications. So far, most of the high-efficiency NW solar cells have been demonstrated in InP NW based systems.^[26, 27] Recently, it has been reported that InP NW array based chemiresistive sensor can achieve high sensitivity, selectivity and long-term stability to NO₂ at room temperature.^[28] Combining their superior photovoltaic properties and NO₂ sensitivity, InP NW array is a promising candidate for self-powered sensing applications. To date, despite that a few different III-V nanowire materials were investigated for gas and biomolecule sensing,^[29-31] they have rarely been demonstrated as self-powered gas sensors.

In this work, we report a novel InP NW array-based gas sensor architecture that combines a PV junction and an active sensing region to achieve highly sensitive, selective, and reproducible self-powered NO₂ sensing at room-temperature. Prior to NW growth, the NW and device structure were designed via numerical simulation that models PV NW sensing mechanisms and optimizes performance. Then axial junction based InP NW arrays were grown according to the simulation optimized structures by the process of selective-area metal-organic vapor-phase epitaxy (SA-MOVPE).^[32] The NW crystal structure and optical

This article is protected by copyright. All rights reserved.

properties were characterized by transmission electron microscopy (TEM), photoluminescence (PL) and time-resolved photoluminescence (TRPL). The NW array sensor devices were designed and fabricated to enable robust contacts for signal extraction, while maintaining a large, exposed NW active area for gas sensing. Without an external power source, the device operates as photovoltaic gas sensor and responds to NO₂ with a high sensitivity, even under a much weaker light intensity than a standard solar illumination. This device also presents a high selectivity, and a sub-ppb level limit of detection (LOD). Finally, we demonstrate that our NW sensor can be readily integrated onto a microchip board for on-field dynamic NO₂ concentration measurements from vehicle exhaust pollutant. Our results pave the way for a miniaturized, power source-free nanoscale sensor platform for future IoT system applications.

2. Results and Discussion

2.1 Device Design and Self-Powered Sensing Mechanism

When applied to gas sensing, the one-dimensional nanoscale NW geometry provides an abundant and engineerable surface area for adsorbing and interacting with gas molecules. For an InP NW array, it is found that once the NO₂ molecules are adsorbed onto the NW surface, the resultant acceptor-like surface states capture electrons from the NW surface,^[28] turning it into a high resistance state and leading to a measurable signal of the adsorbed NO₂. Based on this fundamental mechanism and PV effect attainable by formation of a p-n junction, we have conceptualized an InP NW array PV sensor to achieve gas sensing and self-powered carrier collection simultaneously. Under light illumination, a photocurrent is generated in the p-n junction embedded NWs i.e., a short-circuit current (I_{sc}) without external power supply. NO₂ exposure effectively modulates the photocurrent flowing through the p-n junction due to the charge (electrons) transfer from the NWs to the adsorbed NO₂ molecules, causing notable change to the photocurrent. Therefore, the p-n junction-based sensing response (R) can be defined as:

This article is protected by copyright. All rights reserved.

$$R = \frac{(I_0 - I_{\text{gas}})}{I_0} \times 100\% \quad (1)$$

where I_0 and I_{gas} denote the initial I_{SC} in air and the final I_{SC} in response to gas adsorption, respectively. I_{gas} can be either greater or smaller than I_0 as will be discussed later, leading to either a positive or negative value for the measured R .

To better understand the PV NW sensing mechanism, we investigated and compared two common axial p-n junction structures, based on material growth, which has been extensively studied and optimized in our previous work^[25, 31-33]: NW array with i-(intrinsic) and n-doped segments grown on a p-doped InP substrate, referred as p-i-n hereafter (**Figure 1a**), and NW array with i-(intrinsic) and p-doped segments grown on a n-doped InP substrate, referred as n-i-p hereafter (Figure 1b). To allow effective gas sensing and NW top contact for signal extraction, a light illumination window is created at the top of the NW for gas exposure (Figure 1a). Considering the mechanical stability of the NW array, the size of the exposure window cannot be too large. The length of the whole exposed NW is set to be 700 nm (500 nm of the doping segment and 200 nm of the exposure window depth) in the simulation, which is a realistic size that can be achieved reliably by device fabrication. By varying the top i-n or i-p junction depth of these two types of NW structures shown in Figure 1a, b, we simulated I_{SC} before and after gas exposure to calculate sensing response by Equation 1 using COMSOL Multiphysics (see Table S1 and Figure S1 in Supporting Information (SI) for details of model setup).

It was found that the relative position of i-n or i-p junction with respect to the exposure window played a critical role in sensing performance, as plotted in Figure 1c, d, respectively. For the p-i-n structure, large positive responses are obtained as shown in Figure 1c, whereas for the n-i-p structure, the response changes from positive to negative within a small range of values with the junction depth increasing as shown in Figure 1d. The polarity of the sensing response for different structures can be explained with the aid of a band diagram of the NW top junction (Figure 1e, f), where the case of n-/p-doped top segment length is set to 450 nm. For the case of a p-i-n structure under illumination, NO_2 gas molecules adsorbed on the top n-doped segment and i-region of the NW (lightly n-doped due to background impurity doping during SA-MOVPE growth, based on

This article is protected by copyright. All rights reserved.

experimental data^[33]) will form surface states that act as electron acceptors, giving rise to an upward surface band bending as shown in Figure 1e.^[34-35] As a result, the majority carrier (i.e. electron) concentration in both the top n-doped segment and the i-region is reduced, leading to a decreased photocurrent and hence a positive sensing response as calculated by Equation 1. Since the top n-segment is highly doped to $3 \times 10^{18} \text{ cm}^{-3}$, the corresponding band bending (and carrier depletion) is much less evident than that of the i-segment when subjected to same amount of gas adsorption. Therefore, the sensing response of p-i-n structure decreases sharply as the top n-segment length increases and becomes longer than exposure window such that no i-segment is exposed for sensing, since most carrier depletion occurs within the i-layer.

When a n-i-p NW sensor is exposed to NO_2 , the resultant upward band bending (Figure. 1f) in the top p-doped segment increases the majority carrier (i.e., hole) concentration and thus the photocurrent shows an enhancement, whereas in the i-region the band bending depletes the majority carriers (i.e., electron), leading to a decreased photocurrent in contrast to the p-segment. For a shallow i-p junction as in Figure 1f, due to the large band bending in the i-segment, electron depletion plays a dominant role compared to the hole enhancement in the top p-doped segment. The net effect is a decreased photocurrent and positive sensing response. As the junction depth increases, the hole concentration enhancement becomes increasingly larger, which eventually leads to increased photocurrent and thus a negative sensing response. By comparing the response curves for the two structures, the p-i-n based device is a better candidate for high-performance oxidative gas sensing. The length of top n-segment plays a critical role, which should be kept as short as possible just for the electrical contact, so that the i-region can be sufficiently exposed for a better sensing performance. For the n-i-p structure, varying the junction depth plays limited role due to its bipolar sensing response in top p-segment and i-region. As a result, the absolute response value is less than 5% with all junction depths considered.

This article is protected by copyright. All rights reserved.

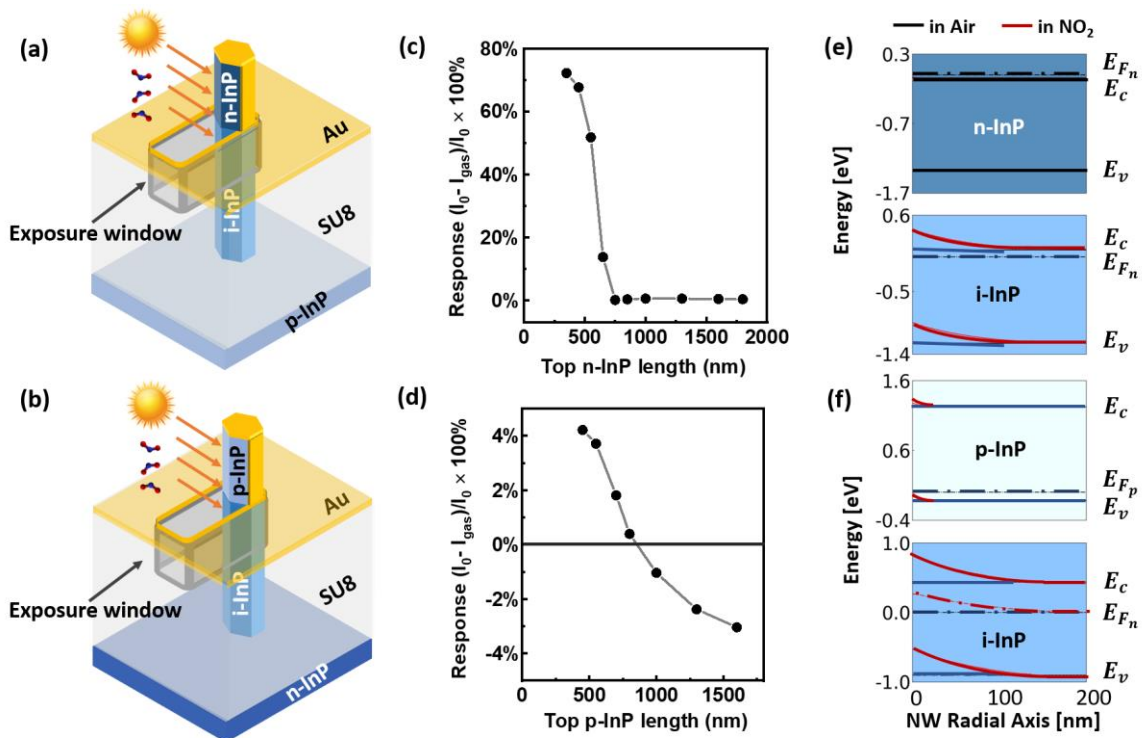


Figure 1. (a, b) Three-dimensional schematic of a unit cell of a p-i-n and a n-i-p NW based sensor, respectively. (c, d) Simulated gas sensing response vs. NW top segment length. (e, f) Band diagram of the respective structures before (i.e., in air) and after gas exposure (i.e., in NO₂).

2.2 Experimental Results and Discussion

To confirm the simulation results, two types of axial homo-junction InP NW structures, p-i-n and n-i-p, illustrated in **Figure 2a** and e, were grown by SA-MOVPE (see details in Experimental Section and Figure S2, SI) under the same conditions as reported previously.^[34] The scanning electron microscope (SEM) images are illustrated in Figure 2b, c, f, and g, showing well-ordered InP NWs with a taper-free hexagonal cylinder shape. The two structures display a similar configuration due to the same growth time and substrate pattern design, with a diameter of around 110 nm, a length of 3-4 μm, and an inter-spacing of 600 nm. The crystal structure is determined by transmission electron microscopy (TEM) analysis, confirming a pure wurtzite crystalline structure (Figure S3 in SI).

A

This article is protected by copyright. All rights reserved.

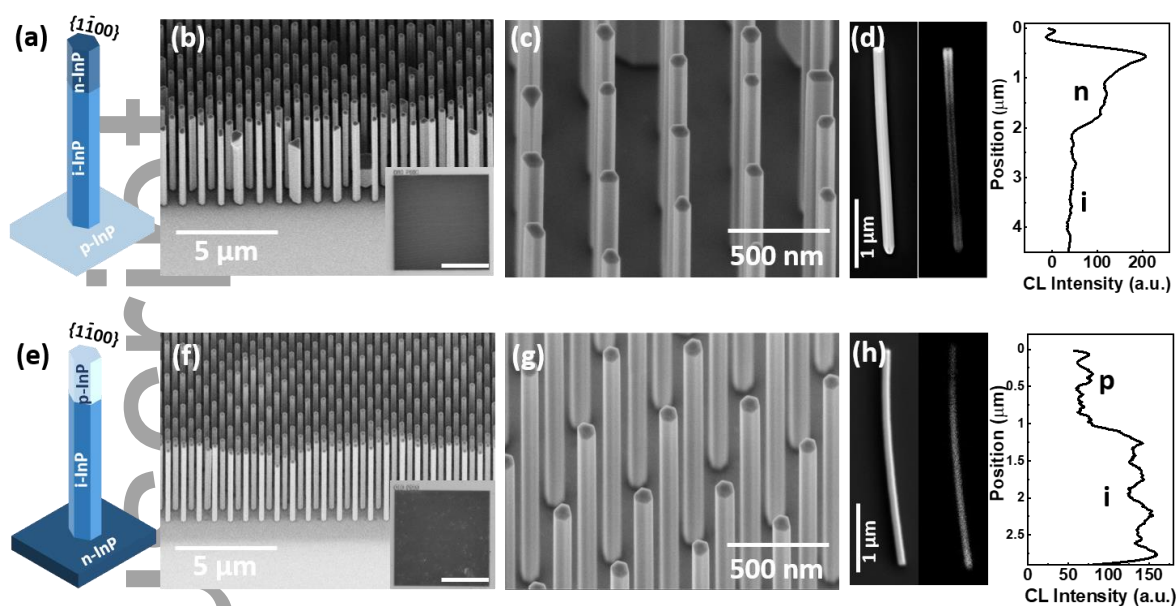


Figure 2. (a, b, c) Schematic and SEM images of i-n InP NW on p-doped InP substrate (p-i-n). (e, f, g) Schematic and SEM images of i-p InP NW on n-doped InP substrate (n-i-p). (d, h) SEM and corresponding cathodoluminescence (CL) image with CL intensity profile of p-i-n and n-i-p InP NW, respectively.

The doping profiles of the two NW structures were characterized by cathodoluminescence (CL) of single NWs,^[32] transferred from NW arrays to a Si substrate, as shown in Figure 2d, h, clearly indicating the two different doping segments within these two structures. The bright-and-dark contrast of the CL panchromatic image^[36] arises from the different doping type and level of NW along the axial direction. Figure 2d shows that the n-segment has a much stronger luminescence than the i-segment, due to a higher electron concentration, which increases the transition probability of a donor-valence band transition, in comparison to an intrinsic-valence band transition. While for the p-doped top segment (Figure 2f), the transition probability of an acceptor-valence band transition is lower than that of an intrinsic-valence band transition, leading to a lower luminescence in the p-segment than that of the i-segment. The SEM-CL characterization indicates that both n-i-p and p-i-n structures grown by the SA-MOVPE method present well-defined junctions. The NWs were also transferred to a SiO₂/Si substrate for photoluminescence (PL) and time-resolved

This article is protected by copyright. All rights reserved.

photoluminescence (TRPL) measurements (Figure S4, SI). It is found that the lifetimes of i-p and i-n nanowire segments are $\sim 0.7 - 0.4$ ns and $\sim 0.3 - 0.1$ ns, respectively. Although these values are lower than the best lifetime values reported previously by our group,^[33] it is adequate to realize photovoltaic effect (Figure 3) for the self-powered sensing application.

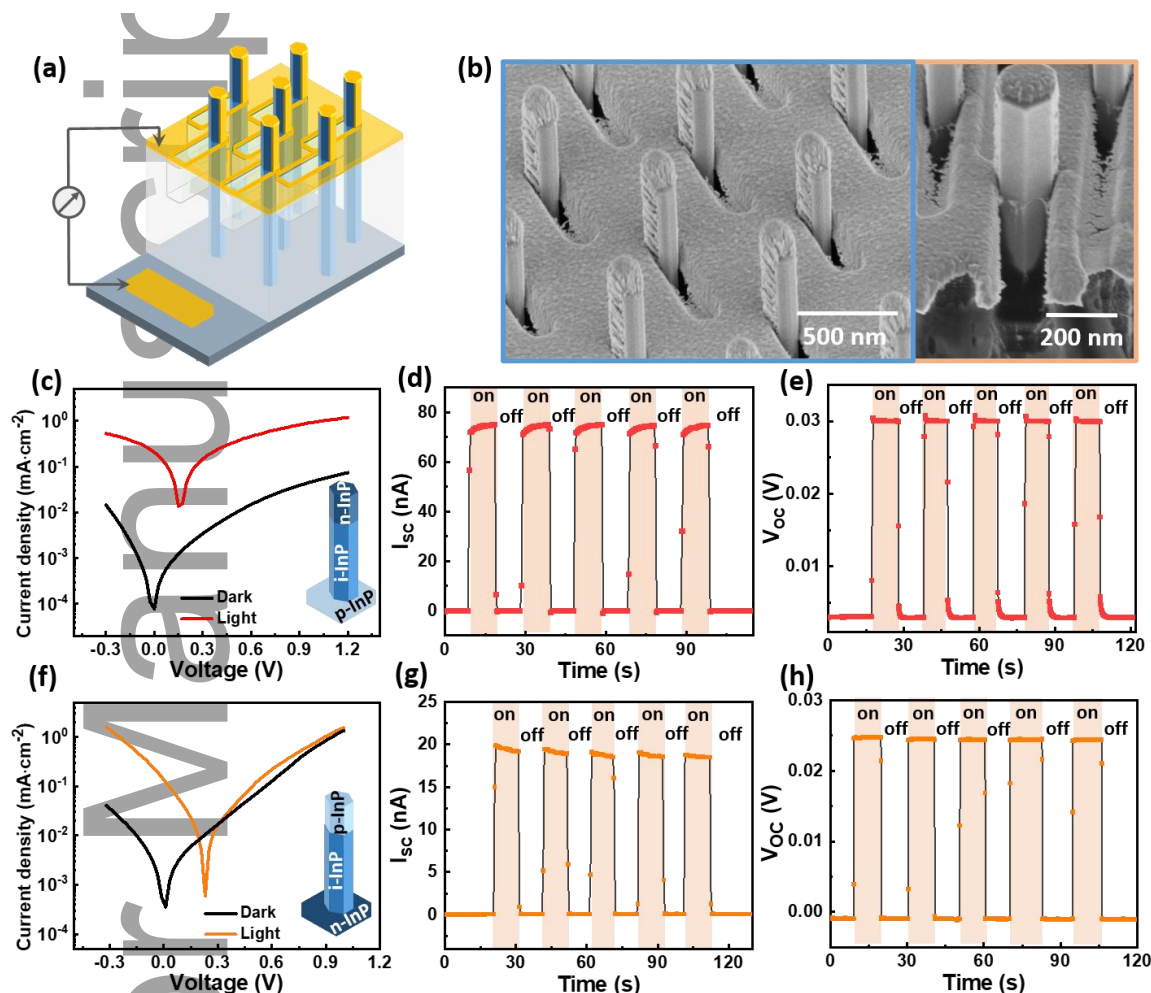



Figure 3. (a) Schematic of as-fabricated InP NW array sensor. (b) SEM image from the top of the device, with a cross-sectional view highlighting the window at the top junction region opened for gas sensing (right panel). (c, f) Dark/light I–V characteristics of the p-i-n and n-i-p InP NW arrays (light source: solar simulator @AM1.5, 42.3 mW·cm⁻²). (d, g) Time-dependent short-circuit current (I_{sc}) of p-i-n and n-i-p InP NW device, respectively; ‘on’ and ‘off’ correspond to the states with and without illumination. (e, h)

This article is protected by copyright. All rights reserved.

Time-dependent open-circuit voltage (V_{OC}) of p-i-n and n-i-p InP NW device, respectively.



For the photovoltaic and sensing characterization, the as-grown NW arrays were then fabricated into an innovative NW PV sensor structure as illustrated in **Figure 3a**, by planarization (with polymer SU8-5), tilt-angle metal contact deposition^[28] and gas exposure window opening steps (detailed in Experimental Section and Figure S5, SI). It is worth noting that based on the insight from our simulation, we found that the length of the window structure is critical for high sensing performance. A long exposed i-region will maximize the NW surface interaction with the target gas molecules and thus the sensing response insight from the simulation result. Figure 3b presents the SEM images of a fabricated sensor, showing that this novel design has been successfully implemented with the top NW side wall partially covered with metal for electrical contact and the other part exposed in air for gas sensing. The exposure window at the top of NW was successfully obtained through carefully tailoring the Inductively Coupled Plasma (ICP) etching process (details in Experimental Section), to achieve an average exposure length of $\sim 700 \pm 50$ nm. The 50 nm variation is estimated by measuring over 50 NWs by SEM from the fabricated NW array device, which is difficult to avoid due to fabrication induced non-uniformity.

The electrical property of two NW device structures (p-i-n and n-i-p) was characterized by standard dark/light current-voltage (I - V) measurements as shown in Figure 3c and f. The dark I - V curves of both devices show the typical diode characteristic. When illuminated under solar simulator @AM1.5 at a power of $42.3 \text{ mW}\cdot\text{cm}^{-2}$, both devices show PV behavior, indicating successful device fabrication. The p-i-n and n-i-p structures have an I_{SC} density of 0.19 and 0.13 $\text{mA}\cdot\text{cm}^{-2}$ (device area of $200 \times 200 \mu\text{m}^2$), and an open-circuit voltage (V_{OC}) of 0.16 and 0.25 V, respectively. The time-dependent photo-responses are shown in Figure 3d, g and Figure 3e, h for I_{SC} and V_{OC} , where distinct 'ON' and 'OFF' PV states can be well manipulated to fit into the subsequent self-powered gas sensing measurements.



This article is protected by copyright. All rights reserved.

2.3 Laboratory Self-Powered Gas Sensing Performance

Sensing performance was characterized by detecting NO₂ in a gas sensing setup schematically illustrated in **Figure 4**. (a) Schematic of self-powered sensing measurement setup under illumination of a solar simulator @AM1.5. (b) Time-dependent response measured from a p-i-n device under different illumination intensities. The averaged time-dependent sensing response and standard deviation range under a light intensity of 42.3 mW·cm⁻² is shown as the shaded area. (c) Summarized NO₂ concentration vs. calculated response for p-i-n and n-i-p NW structures. The inset shows an enlarged graph of p-i-n sensing responses to 1-10 ppb NO₂. Sensing response measured from (d, e) p-i-n, and (g, h) n-i-p NW structures for different range of NO₂ concentrations. (f, i) Target gas selectivity measurement of p-i-n (f) and n-i-p (i) NW structure, respectively, with a gas concentration of 1 ppm for methanol, methyl nitrides, acetone, ethanol, propane, CO₂, and NO₂. The sensing measurements in (d-i) were performed under light intensity of 42.3 mW·cm⁻². The gas sensing chamber was configured to be illuminated by a solar simulator (with conditions equivalent to where the light I-V characteristics were measured) at zero bias to characterize self-powered sensing performance. Prior to gas injection, the device was placed in the gas sensing chamber with illumination and constant air flow to generate steady-state I_{SC} . As the NO₂ gas injection started, I_{SC} either decreased or increased, depending on the device structure as discussed earlier, and then reached a saturation. When NO₂ gas was switched off and air flow was resumed, I_{SC} recovered back to the initial base level. Utilizing the variation of I_{SC} as a sensing signal, the NO₂ sensing R was then calculated according to Equation 1.

To find out the threshold light intensity for our self-powered NW sensor operation and the capacity of the device working under various illumination conditions, the p-i-n device was measured under a series of attenuated light intensities tuned by a neutral density filter. Figure 4b shows that with 100 ppb NO₂, the R value was consistent within the standard deviation range of R ($22 \pm 4.9\%$, for 10 cycles of sensing measurement) under a series of decreased light intensities from the original level 42.3 mW·cm⁻² (shaded area), even when the light intensity was decreased to 10% of its original level (or <5% 1-sun condition). Under the reduced light intensity, the baseline I_{SC} (i.e., I_0) and the gas

This article is protected by copyright. All rights reserved.

adsorption induced I_{SC} (i.e., I_{gas}) decreases simultaneously, such that the R calculated by Equation 1 remains at a similar value. Such light-intensity independent performance is highly desirable for sensing in a realistic environment since atmospheric solar irradiation usually varies drastically during the day. Figure 4b also indicates minor variation of sensing response time with the light intensity, which is discussed in Figure S6, SI.

Figure 4. (a) Schematic of self-powered sensing measurement setup under illumination of a solar simulator @AM1.5. (b) Time-dependent response measured from a p-i-n device under different illumination intensities. The averaged time-dependent sensing response and standard deviation range under a light intensity of 42.3 mW·cm⁻² is shown as the shaded area. (c) Summarized NO₂ concentration vs. calculated response for p-i-n and n-i-p NW structures. The inset shows an enlarged graph of p-i-n sensing responses to 1-10 ppb NO₂. Sensing response measured from (d, e) p-i-n, and (g, h) n-i-p NW structures for different range of NO₂ concentrations. (f, i) Target gas selectivity measurement of p-i-n (f) and n-i-p (i) NW structure, respectively, with a gas concentration of 1 ppm for methanol, methyl nitrides, acetone, ethanol, propane, CO₂, and NO₂. The sensing measurements in (d-i) were performed under light intensity of 42.3 mW·cm⁻². d and e show the time-dependent response of the p-i-n device in the concentration range 1 - 1000 ppb. The results from the n-i-p sample are illustrated in Figure 4g and h, with a concentration range of 20 - 1000 ppb. Figure 4. (a) Schematic of self-powered sensing measurement setup under illumination of a solar simulator @AM1.5. (b) Time-dependent response measured from a p-i-n device under different illumination intensities. The averaged time-dependent sensing response and standard deviation range under a light intensity of 42.3 mW·cm⁻² is shown as the shaded area. (c) Summarized NO₂ concentration vs. calculated response for p-i-n and n-i-p NW structures. The inset shows an enlarged graph of p-i-n sensing responses to 1-10 ppb NO₂. Sensing response measured from (d, e) p-i-n, and (g, h) n-i-p NW structures for different range of NO₂ concentrations. (f, i) Target gas selectivity measurement of p-i-n (f) and n-i-p (i) NW structure, respectively, with a gas concentration of 1 ppm for methanol, methyl nitrides, acetone, ethanol, propane, CO₂, and NO₂. The sensing measurements in (d-i) were performed under light intensity of 42.3 mW·cm⁻². c summarizes the corresponding concentration-dependent sensing response for both p-i-n and n-i-p samples with their linear-fitting slope (L) which



This article is protected by copyright. All rights reserved.

is defined as device sensitivity, marking the sensor output signal changes with unit analytes input. It is noticeable that the absolute value of response at 1000 ppb and the device sensitivity for n-i-p structure (15.9%, 0.014%/ppb) is much smaller than those of p-i-n structure (84.1%, 0.62 %/ppb), verifying the results of the numerical simulation that predicts the NW with unipolar sensing response from i-n top junction is superior to the bipolar one from i-p junction. According to the aforementioned sensing mechanism in section 2.1, I_{SC} of the n-i-p structure increases with NO_2 injection, thus giving a negative sensing response, in contrast to the decreasing I_{SC} and a positive sensing response from the p-i-n structure.^[39, 40]

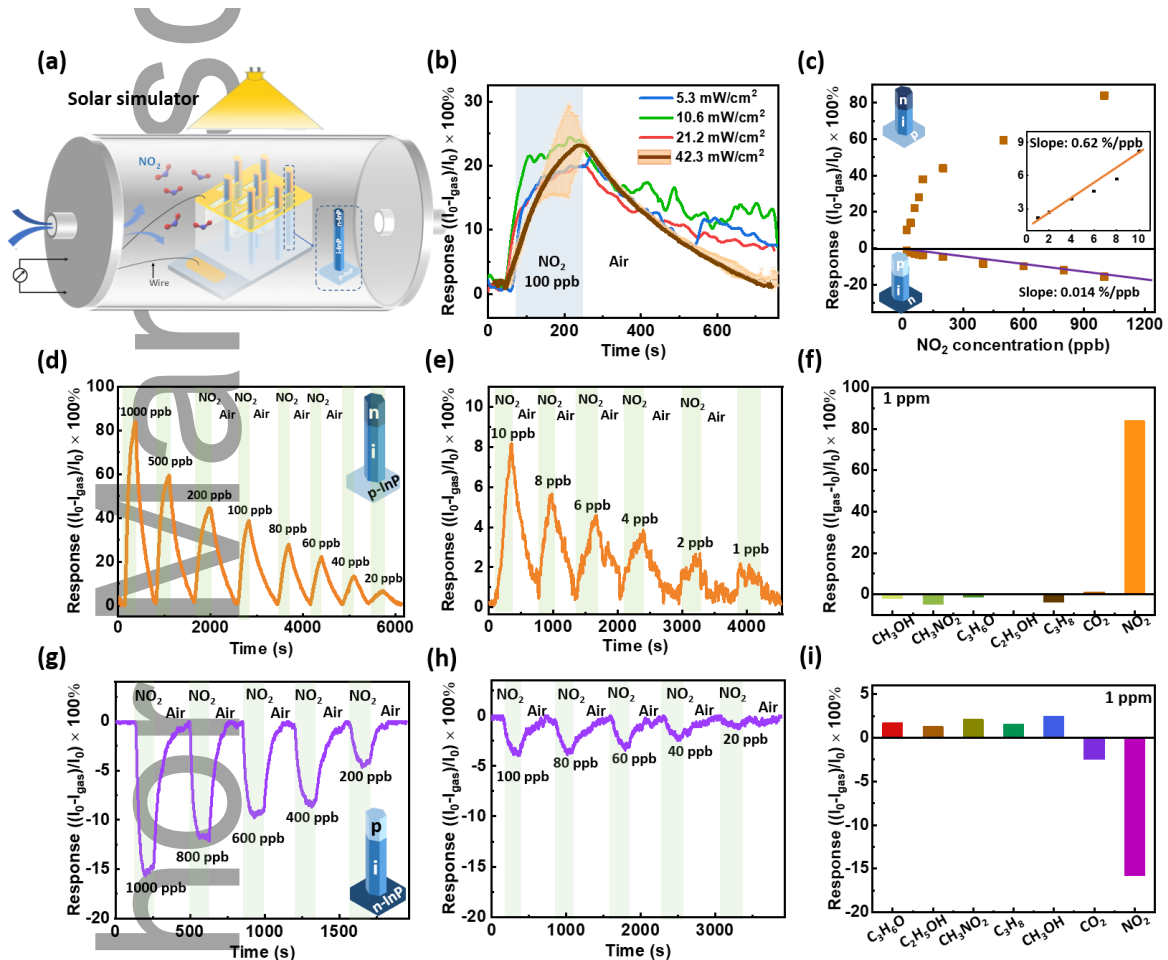


Figure 4. (a) Schematic of self-powered sensing measurement setup under illumination of a solar simulator @ AM1.5. (b) Time-dependent response measured from a p-i-n device under different illumination intensities. The averaged time-dependent sensing response and standard

This article is protected by copyright. All rights reserved.

deviation range under a light intensity of $42.3 \text{ mW}\cdot\text{cm}^{-2}$ is shown as the shaded area. (c) Summarized NO_2 concentration vs. calculated response for p-i-n and n-i-p NW structures. The inset shows an enlarged graph of p-i-n sensing responses to 1-10 ppb NO_2 . Sensing response measured from (d, e) p-i-n, and (g, h) n-i-p NW structures for different range of NO_2 concentrations. (f, i) Target gas selectivity measurement of p-i-n (f) and n-i-p (i) NW structure, respectively, with a gas concentration of 1 ppm for methanol, methyl nitrides, acetone, ethanol, propane, CO_2 , and NO_2 . The sensing measurements in (d-i) were performed under light intensity of $42.3 \text{ mW}\cdot\text{cm}^{-2}$.

From Figure 4. (a) Schematic of self-powered sensing measurement setup under illumination of a solar simulator @AM1.5. (b) Time-dependent response measured from a p-i-n device under different illumination intensities. The averaged time-dependent sensing response and standard deviation range under a light intensity of $42.3 \text{ mW}\cdot\text{cm}^{-2}$ is shown as the shaded area. (c) Summarized NO_2 concentration vs. calculated response for p-i-n and n-i-p NW structures. The inset shows an enlarged graph of p-i-n sensing responses to 1-10 ppb NO_2 . Sensing response measured from (d, e) p-i-n, and (g, h) n-i-p NW structures for different range of NO_2 concentrations. (f, i) Target gas selectivity measurement of p-i-n (f) and n-i-p (i) NW structure, respectively, with a gas concentration of 1 ppm for methanol, methyl nitrides, acetone, ethanol, propane, CO_2 , and NO_2 . The sensing measurements in (d-i) were performed under light intensity of $42.3 \text{ mW}\cdot\text{cm}^{-2}$. d and g, it is noted the extracted response time of the n-i-p device ($\sim 50 \text{ s}$) is shorter than that of the p-i-n device ($\sim 140 \text{ s}$). This difference mainly results from two factors: i) the transient photocurrent change is intrinsically limited by the drift of photo-generated carriers within the exposure window, which is directly proportional to the built-in electric field formed near the top i-n or i-p junction as determined by their doping profiles. The electric field distribution for the two junction regions can be found in Figure S7 in SI, which implies that the carrier drift velocity in n-i-p structure is larger than that in the p-i-n structure, leading to a faster transient photocurrent change and thus a shorter response time; ii) different doping type (Si and Zn) in the top n/p segment of two NW structures may also result in different surface activation energy, thereby changing the reaction rate constant as gas particles interact with the NW surface and affecting the response time.^[41, 42]



This article is protected by copyright. All rights reserved.

For the more sensitive p-i-n structure, a linear correlation of response versus concentration can be observed at two separate concentration regimes, with a smaller slope at the high concentration range (>100 ppb). This phenomenon also exists in previously reported work, which indicates that the sensor saturates gradually due to the limited number of surface adsorption sites.^[22, 37] The superior sensitivity performance of the p-i-n structure is also indicated by the measurement of an extremely low NO₂ concentration (1 ppb), where a distinguishable sensing response of 2% can still be obtained as shown in Figure 4. (a) Schematic of self-powered sensing measurement setup under illumination of a solar simulator @AM1.5. (b) Time-dependent response measured from a p-i-n device under different illumination intensities. The averaged time-dependent sensing response and standard deviation range under a light intensity of 42.3 mW·cm⁻² is shown as the shaded area. (c) Summarized NO₂ concentration vs. calculated response for p-i-n and n-i-p NW structures. The inset shows an enlarged graph of p-i-n sensing responses to 1-10 ppb NO₂. Sensing response measured from (d, e) p-i-n, and (g, h) n-i-p NW structures for different range of NO₂ concentrations. (f, i) Target gas selectivity measurement of p-i-n (f) and n-i-p (i) NW structure, respectively, with a gas concentration of 1 ppm for methanol, methyl nitrides, acetone, ethanol, propane, CO₂, and NO₂. The sensing measurements in (d-i) were performed under light intensity of 42.3 mW·cm⁻².e. Based on the classification of International Union of Pure and Applied Chemistry,^[38] limit of detection (LOD) is defined as a concentration of the analyte which causes a response 3 times higher than the noise level of the device (*i.e.*, in the absence of the analyte), *i.e.* $LOD = 3 \times (RMS_{noise}/L)$. Gas sensor noise was calculated via root-mean-square deviation (RMS_{noise}) processing from 100 consecutive baseline data points taken under the exposure to air.^[39] From the baseline in Figure 4e, the $RMS_{noise} = 0.10\%$ and $L = 0.62\%/ppb$ (obtained from the inset of Figure 4c), so the calculated LOD is 0.49 ppb, which is the lowest record achieved by a self-powered gas sensor to the best of our knowledge. Also, the effect of humidity on this p-i-n sensor was investigated under various relative humidity (RH) levels (Figure S8, SI). It was found that even with a high concentration of water vapor (RH 65%), the NW sensor maintains its high sensitivity despite a small degradation in sensing response (< 30%) compared to the dry condition (RH 0%), demonstrating excellent humidity tolerance.

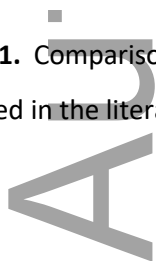


This article is protected by copyright. All rights reserved.

To investigate the device reproducibility, the better performing p-i-n device was repeatedly exposed to NO₂ (at the same concentration) and we observed a consistent sensing response for an extended period of time (Figure S9c, d in SI). Furthermore, both the n-i-p and p-i-n structured devices demonstrated a high selectivity to NO₂ as shown in Figure 4f and 4i. At 1 ppm level, the sensing response of these two devices to other organic vapors and common atmosphere gases (methanol (CH₃OH), ethanol (C₂H₅OH), methyl nitrite (CH₃NO₂), carbon dioxide (CO₂) and propane (C₃H₈)) are negligible compared to NO₂. Besides I_{SC} , the time-dependent V_{OC} can be also measured as an alternative readout signal that can be useful for integration with a digital microchip circuit board, as demonstrated in Figure S9 and S10 in SI.^[13] The V_{OC} sensing response measured from both the p-i-n and n-i-p NW sensors presents similar characteristics to what was observed with I_{SC} , i.e., the magnitude of the sensing response is concentration dependent, and V_{OC} decreases (increases) similarly when exposed to NO₂ for the p-i-n (n-i-p) structure.

Compared with different types of recently reported self-powered gas-sensing devices as summarized in **Table 1**, our p-i-n InP NW NO₂ sensor shows an overall outstanding performance with a high response (84%/ppm), the lowest LOD (~0.49 ppb), and an ability to work stably under a natural light source with varied intensity at room temperature. The NW sensor's performance reported here is also comparable to the best reported non-self-powered sensors^[43, 44] taking into consideration of the operation conditions, which are important figures of merit for practical applications. For example, as summarized in **Table S2**, a well-designed layer-like WO₃ sensor can achieve lower limit of detection of 0.243 ppb, but required a high operation temperature of 160 °C.^[43] A single-layer MoS₂ based device has realized a sensitivity up to 4.9%/ppb and limit of detection of 0.1 ppb,^[44] but required intense red LED illumination (60.9 mW/cm²) to enhance the conductivity of the MoS₂ channel and thus the NO₂ sensing response.

Table 1. Comparison of typical sensing performance parameters from self-powered gas sensors reported in the literature (room temperature operation).



This article is protected by copyright. All rights reserved.

Device structure	Light source	Measured signal	Target gas (LOD)	Response 100% (gas concentration)	Response/recovery time (s)	Ref
p-i-n InP NW	Solar simulator (AM 1.5)	I_{sc} (nA) V_{oc} (mV)	NO ₂ (0.49 ppb)	84% (1 ppm)	200 / 400	This work
p-Si/n-ZnO (amine-/thiol-functionalization)	Solar simulator (AM 1.5)	V_{oc} (mV)	NO ₂ (170 ppb)	Amine: 7.5% Thiol: 9.8% (250 ppb)	~1000	[15]
CNT-SiNW	Solar simulator (AM 1.5)	V_{oc} (V)	NO ₂ (10 ppm)	46% (10 ppm)	4-6	[17]
SWNTs/Si	$\lambda = 600$ nm, $P = 1.8$ mW cm ⁻²	V_{oc} (mV)	NO ₂ (100 ppb)	2.23% (400 ppb)	~50	[45]
NiO/ZnO/ITO	Solar simulator 100 mW cm ⁻² AM1.5	V_{oc} (V)	CO ₂	0.1%	150/100	[46]
CsPbBr ₃	Solar simulator (AM 1.5)	I_{sc} (nA)	Acetone (1 ppm)	3% (1 ppm)	10/5	[16]
CsPbBr ₂ I	Solar simulator (AM 1.5)	I_{sc} (nA)	Acetone (1 ppm)	16% (1 ppm)	150	[47]
Gr/WS ₂ /Gr	White light $P = 100$ mW cm ⁻²	I_{sc} (μ A) or V_{oc} (mV)	NO ₂ (5ppm), H ₂ (50ppm)	NO ₂ : 70% (5ppm), H ₂ : 17% (50ppm)	~500	[14]
SiNWs/ITO	Red LED $\lambda = 576$ nm, $P = 20$ mW cm ⁻²	I_{sc} (μ A)	NO ₂ (5ppb)	90% (1 ppm)	80/850	[41]
Au@rGO/GaN nanorods	UV LED $\lambda = 382$ nm, $P = 1.71$ mW cm ⁻²	I_{sc} (μ A)	CO (5 ppm)	38% (20 ppm)	400/1000	[48]
FMCPiB	Solar simulator (AM 1.5)	I_{sc} (nA)	NO ₂ (1 ppm)	8% (8 ppm)	17/126	[49]

This article is protected by copyright. All rights reserved.

2.4 On-Field Gas Sensing

Based on the laboratory sensing measurement results, the p-i-n NW sensor was chosen to confirm its applicability in a realistic environment. A real-time on-field measurement was enabled by connecting our NW device to a portable microprocessor with a USB interface (JLM Innovation with supplementary software JLMlogSP), where the electrical signal generated by the NW sensor is transmitted and processed. A prototype workflow from the on-field sensing measurement to the data analysis and output result is illustrated in **Figure 5**. Prior to on-field operation, a sensor calibration in self-powering mode was demonstrated, as shown in Figure 5a, which correlates the sensing response value with the NO₂ concentration. This calibration was performed in a laboratory gas sensing setup where the injected gas concentration was known and can be precisely controlled (Figure S11). However, when the NW sensor was connected to the portable USB microprocessor, it could no longer be fitted into the same sensing setup. In this case, the calibration was then performed in a home-made 3D-printing enclosure (with an LED light source) that can accommodate the NW sensor integrated on the USB system. In this case, the enclosure was not completely sealed and isolated from the ambient atmosphere as in a standard gas sensing chamber. Hence, the measured sensing response tends to overestimate the injected gas concentration (i.e., consider a small amount of gas leakage). The calibration performed with the portable USB microprocessor locates the boundary of such an overestimation. Therefore, it is expected that a real measurement result from a vehicle exhaust should fall in between the two calibration lines as indicated by the pink shaded area.

The portable NW sensor system was then brought to the realistic environment for on-field measurement with the exposure of a 4-cylinder gasoline car exhaust (Figure 5b). An example time-dependent response curve shows that the value and shape of response pulse vary in different accelerator pedal pressing duration and revolutions per minute (RPM) of the engine, as NO₂ concentration in the exhaust gas depends on these parameters. The measured response curve, together with the calibration results, was transmitted to a data evaluation unit (e.g., a laptop, or an embedded system with USB or Bluetooth interface) for processing. Here we

This article is protected by copyright. All rights reserved.

demonstrate a simple pipeline of data acquisition and processing (Figure 5c) for a vehicle exhaust at 2500 RPM where the gas pedal was pressed four times, each of which lasted approximately 25 s. The raw data from the measurement was then evaluated with a logistic filter to remove noise (a double-logistic filter in this demonstration) to extract sensing response value.

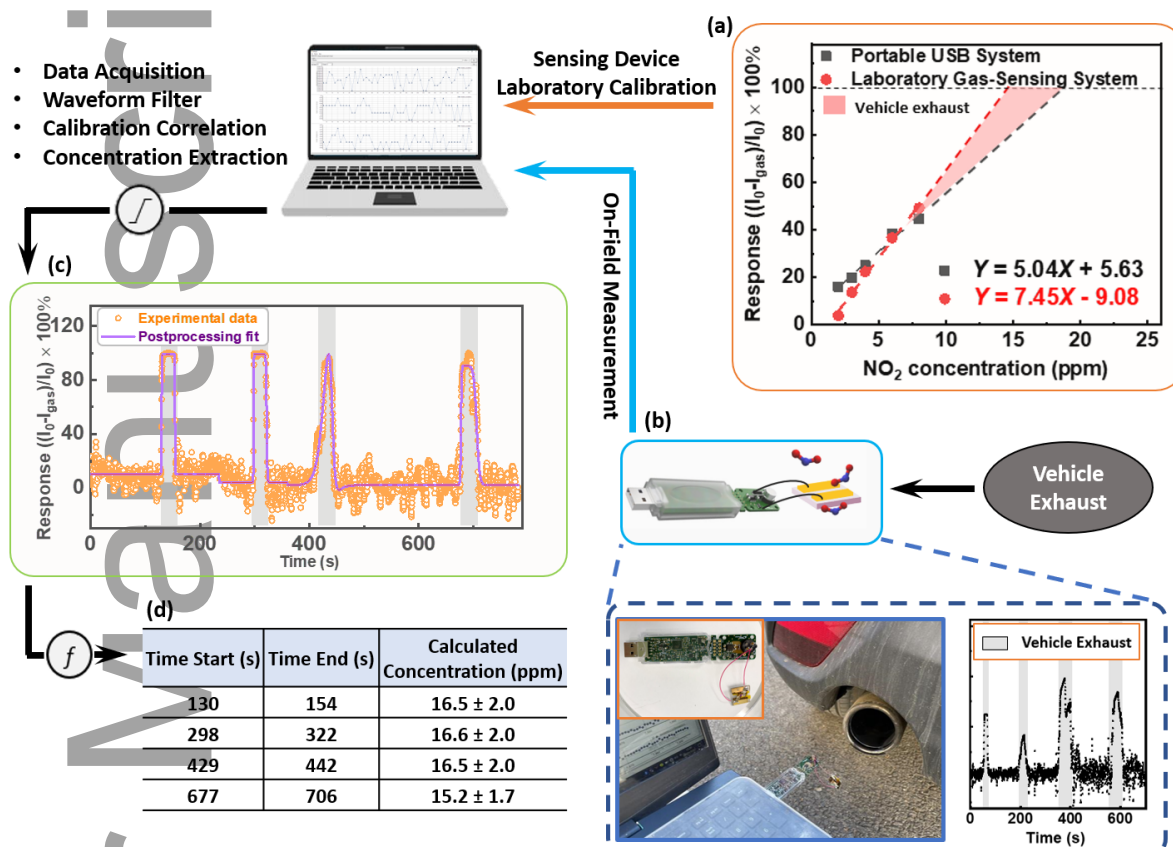



Figure 4. A prototype workflow for practical on-field gas sensing measurement. (a) The NW sensor concentration calibration in a laboratory environment (portable USB microprocessor system and laboratory gas sensing system). (b) The schematic and on-site photos of the on-field vehicle exhaust measurement based on the NW sensor integrated with the USB interface and an example of acquired data. (c) Data measured by this USB interface and the corresponding post-processed fitting result by user-specified data filters to remove noise and extract sensing response values; (d) By

correlating with the laboratory calibration, the NO₂ concentration can be dynamically monitored.



It is worth mentioning that in addition to NO₂, there are also small amount of carbon monoxide (CO), nitrogen monoxide (NO), sulfur dioxide (SO₂), formaldehyde (HCHO), and benzene (C₆H₆) contained in the car exhaust.^[50] However, they may have negligible effects on the NO₂ sensing results due to their weak or non-oxidizing nature. As indicated in Figure 4f, the InP NW sensor only produces a large positive sensing response to the highly oxidising NO₂ due to its high electron affinity, with negligible responses to CO₂ (weak oxidising gas) and other reducing gases including acetone, propane, and ethanol. For the aforementioned gases in the car exhaust, CO and other hydrocarbons are reducing gases, while NO and SO₂ have a much smaller electron affinity (NO: 0.025 eV; SO₂ 1.10 eV) than that of NO₂ (2.27 eV). Moreover, the effects of those weak or non-oxidizing gases on crystalline InP structure have been investigated previously. Wencai, Y. et al. constructed a model of two-dimensional InP monolayer to calculate the electron charge transfer (Q) and absorption energy (E_a) of CO, NO, and NO₂ by *ab initio* density functional theory (DFT),^[51] which found that the Q and E_a of NO₂ (0.588 e, 1.299 eV) on the InP surface are much larger than those of CO and NO (CO: 0.035 e, 0.17 eV; NO: 0.312 e, 0.641 eV). The larger Q and E_a of NO₂ indicate that it has a significantly stronger chemical adsorption and charge transfer ability with InP than those of CO and NO. The experimental studies from Kostryukov, V. F. et al.^[52] and Garcia, M. A. et al.^[53] also demonstrated that InP thin film has a much smaller sensing response to CO and NO than to NO₂. Furthermore, according to the study from Christian, W. et al,^[54] and Parthasarathi, B. et al,^[55] the concentration of hydrocarbons and SO₂ in vehicle exhaust is much smaller than that of NO₂ (NO₂ is ~ 0.4 g·km⁻¹; hydrocarbons in total is ~0.1 g·km⁻¹; SO₂ only shows possible trace from vehicle emission). Therefore, it is reasonable to conclude that the presence of a mixture of other interfering gases has negligible impact on the NO₂ monitoring results in our on-field vehicle exhaust measurements.

The calculated NO₂ concentration from this p-i-n NW sensor on-field measurement is ~15.2-16.6 ppm, which is in good agreement with the result measured from a commercial NO₂ air quality sensor



This article is protected by copyright. All rights reserved.

(~8.9-13.0 ppm, Figure S12, SI), as well as previously reported studies (10.0-50.0 ppm from optical fiber sensors^[56] and 15.0-16.9 ppm from chemiluminescence^[57]), indicating the practical functionality and accuracy of our self-powered NW sensor system.

To improve the device performance and functionalities, the p-i-n structure can be further optimized by reducing n-segment length and increasing i-segment length to enhance its sensitivity. Apart from the axial p-n junction, it may be worth investigating a radial-junction p-n NW structure, which could provide a larger junction region and simplify the device fabrication process. Furthermore, multiple NW arrays with varied pitch sizes and diameters can be grown during the same epitaxial growth sequence to provide multi-channel detection, which could further enhance the dynamic range of the NO₂ detection.

3. Conclusion

In this work, a novel self-powered sensor architecture was successfully designed and demonstrated based on bottom-up grown p-n homojunction InP NW arrays. We designed the p-n junction-based NW sensor structure and explored the sensing mechanism via numerical simulation. The fabricated sensors based on the p-i-n junction InP NW array show excellent sensitivity with a limit of detection down to the sub-ppb level and a high selectivity to NO₂ in self-powered operation mode. These results promise a new family of self-powered sensing platforms to achieve high-performance gas sensors with a strong environmental fidelity enabled by photovoltaic effect. The integration of the NW sensor with a portable USB interface for practical dynamic on-field measurement is further demonstrated, precisely quantifying NO₂ concentration from a motor vehicle exhaust. Our prototype InP PV NW sensor design paves the way towards a battery-free, highly integrable and compatible sensing platform for applications such as environmental monitoring, industrial safety and hazard alarming. It is a promising step forward to creating a next-generation sensing network for the Internet of Things.

This article is protected by copyright. All rights reserved.

4. Experimental Section

Numerical simulation: The gas sensing simulation was performed using the semiconductor module of COMSOL Multiphysics. To ensure timely convergence of simulated processes, only a 2D equivalent unit cell of nanowire array device, consisting of a single NW, was constructed in simulation. The 3D view, together with the 2D simulation geometry of the unit cell is illustrated in Figure S1 in SI. The exposure window is fixed at 700 nm measured from the top of NWs, while the junction depth is varied from 350 nm to 1800 nm. The left surface within this window is subject to gas exposure, for which a negative surface charge boundary condition is applied to model oxidative NO₂ adsorption. The light generation is only enabled within the window, below which is considered negligible since light is largely blocked by metal contact (Figure 1). The top horizontal boundary, together with right side boundary (300 nm from the top), is set as Ohmic contact to replicate realistic device structure. All simulation related parameters are summarized in Table S1 in SI.

p-i-n / n-i-p junction InP NW growth: (1) Substrate processing: Figure S2 illustrates the processes of preparing InP (111)A substrate (both p-doped and n-doped with a concentration of $(0.8-8) \times 10^{18} \text{ cm}^{-3}$) for NW growth. Firstly, a 30 nm SiO₂ layer was deposited on (111)A InP substrate by plasma enhanced chemical vapor deposition (PECVD) at 300 °C, and the thickness was measured by ellipsometry. A negative photoresist AR6200.09 was spin-coated (step 1: 500 rpm 5 s; step 2: 2000 rpm for 60 s) on SiO₂ layer and baked at 150°C for 1 min on hotplate. Then, the resist was exposed by Raith 150 electron beam lithography (EBL) system based on a designed pattern consisting of 200 × 200 μm² hexagonal dot array with a size of 80 nm and pitch of 600 nm. The exposed pattern area in photoresist layer was removed by the corresponding resist developer. After the development of resist, oxygen plasma (RF power: 300 W; 300 sccm O₂ flow; 2 min,) was used to remove the footage residues in the patterned area. The exposed pattern was then etched by RIE to remove the SiO₂ layer on InP substrate (RF power: 20W; 20 sccm CHF₃ flow; 4.5 min). To remove the possible damage on the exposed InP surface during SiO₂ deposition, 10% H₂O₂ was first used to oxidize the InP layer for 2 min followed by etching off the oxide layer with 10 % H₃PO₄ solution for 2 min. These steps were

This article is protected by copyright. All rights reserved.

repeated sequentially for 5 times and then, the sample was immediately transferred into the MOVPE reactor for NW growth.

(2) p-i-n / n-i-p junction InP NW growth: The InP NW arrays were grown in AIXTRON 200/4 MOVPE reactor, operating at a base pressure of 100 mbar, using H₂ as a carrier gas with a total flow of 14.5 l/min. Trimethylindium (TMIn) and phosphine (PH₃) were used as precursors for the group III (In) and group V (P) elements, respectively. Molar fractions of TMIn and PH₃ were set at 9.38×10^{-6} and 7.59×10^{-4} mol/min, respectively, corresponding to a V/III ratio of 80. All samples were hot baked at 750 °C for 10 min under the PH₃ flow and grown for 4 min at 730 °C for undoped segment (i-InP). Then, Silane (SiH₄) and diethylzinc (DEZn) were introduced during the growth of n-doped segment and p-doped segment for 2 min with all the other parameters kept the same as those used for the growth of undoped InP segment. With this two-step growth process, the i-n and i-p InP NW were grown on p-doped and n-doped substrate respectively, to form n-i-p and p-i-n junctions.

InP NW characterization: The morphology of the as-grown InP NW arrays were characterized by scanning electron microscopy (SEM, FEI VERIOS 460) with electron beam voltage of 2 kV and current of 13 pA. The crystal structure is determined by transmission electron microscopy (TEM, JEOL 2100F) analysis of NWs that were directly transferred from the original array to a copper mesh. Cathodoluminescence (CL) technique was applied on single NWs which were transferred from the array to a Si substrate to characterize its optical property. The CL images were acquired from SEM equipped with a Gatan MONO CL4 components under an electron excitation voltage of 10 kV and current of 0.8 nA at room temperature. The NWs were also transferred to a SiO₂/Si substrate for PL and TRPL at room temperature. The PL system is composed of Horiba LabRAM system equipped with confocal optics, a diode pumped solid-state (DPSS) 532 nm laser, and a liquid nitrogen-cooled array InGaAs detector. The laser beam was focused through a 100x microscope objective lens, resulting in a spot size of 0.36 μm (in radius) estimated by vector diffraction calculation. For TRPL, the emission was collected by the same objective lens and detected by a single photon avalanche diode, which was connected to the PicoHarp 300 time-correlated single photon

This article is protected by copyright. All rights reserved.

counting (TCSPC) system. PL spectra were acquired along single NW from top to bottom position.^[3] The minority carrier lifetime in the NWs was extracted from the single exponential fitting of TRPL decay curve.

Fabrication of self-powered InP NW NO₂ sensor: To fabricate a chemiresistive sensor based on InP axial junction NW array, photoresist SU8-5 (Kirsten Hackenbroich) was spin-coated on NW arrays to fully cover the entire NW arrays. Then SU8-5 was etched back by barrel-etcher (PVA Tepla Gigabatch 310 M) with O₂ flow rate of 300 sccm and power of 500 W to expose ~500 nm of the top of InP NWs for subsequent electrical contact. Then the sample was flood exposed under UV illumination and baked at 200 °C to solidify SU8-5. Since the top junction is deeper than 500 nm, the i-segment of NW is embedded in SU8-5, which prevents shorting of the junction and provides necessary mechanical support to the NWs. A 200 nm Au layer was deposited on nanowires using e-beam evaporator for top contact. The samples were mounted on a special holder to enable the tilt-angle deposition to provide not only electrical contact, but also to partially expose the nanowires to allow gas adsorption and sensing.^[28] The tilt-angle deposition leaves a shadow area behind each NW covered by SU8-5, which can be further etched to extend the exposure window below the top junction. The etching rate of Inductively Coupled Plasma (ICP) etching has been well calibrated such that another ~500 nm of SU8-5 was removed precisely as shown in Figure S5g. The SU8-5 layer shadowed by NW during deposition was exposed and subsequently etched by ICP-F, which formed a hole besides each NW. Then, a 200 nm Au layer was deposited on the back of InP substrate as bottom contact.

Electrical characterization: The electrical and photovoltaic properties of InP nanowire array were characterized by current-voltage (I–V) measurements by Keysight system B2902A source/measurement unit, incorporated with a solar simulator.

NO₂ sensing measurement: The gas sensing performance was measured by home-made sensing setup which consists of a Linkam chamber with a sample stage and Au probes for electrical contact, mass flow controllers (MFCs Bronkhorst), a solar simulator and gas cylinders. For the gas sensing measurements, the carrier gas was simulated air with volume ratio of N₂ to O₂ at 4 ($V_{N_2}/V_{O_2} = 4$, N₂ and O₂, BOC gas). The gas flow rate was controlled by MFCs while the total gas flow rate was kept at 1 l/min for ppm level concentration test and 0.5 l/min for sub-ppm level concentration test. For the measurement of analyte gas, volatile organic compounds (VOCs) (ethanol, 9.91 ppm in N₂, Coregas; acetone, 10.1 ppm in N₂, Coregas; methanol, 10 ppm in N₂, BOC gas) or NO₂ gas was diluted to desired concentration before being purged into the chamber.

Statistical Analysis: For PL and TRPL, more than 5 single NWs from p-i-n and n-i-p arrays were measured, respectively. The lifetime data was analyzed by MATLAB. Dark/light I–V characteristics of the p-i-n and n-i-p InP NW arrays in Figure 3 were obtained from more than 3 samples which were tested under the same dark condition and light intensity. The sensing response of p-i-n sample in Figure 4b was tested more than 10 times of sensing measurement cycles and are given in the form of mean \pm standard deviation by Microsoft Excel. The data in Figure 4c were analyzed using the linear fitting function of Origin 2018 (OriginLab Co.) to obtain the slope of concentration dependent sensing response curve, which gives a measure of sensitivity. The fitted linear slope is $Y = 0.62 X + 1.36$ ($r^2 = 0.98$) for p-i-n sample and $Y = -0.014 X + 1.98$ ($r^2 = 0.95$) for n-i-p sample, both with 95% confidence level. For the on-field vehicle exhaust data, more than 5 times of pedaling were measured by the p-i-n InP NW sensor and commercial NO₂ air quality sensor.

Supporting Information

Supporting Information is available from the Wiley Online Library or from the author.

This article is protected by copyright. All rights reserved.

Acknowledgements

The authors acknowledge the financial support from the Australian Research Council. The authors also acknowledge the Australian National Fabrication Facility (ACT node) for facility support. This research was also funded by and has been delivered in partnership with Our Health in Our Hands (OHIOH), a strategic initiative of the Australian National University, which aims at transforming healthcare by developing new personalized health technologies and solutions in collaboration with patients, clinicians, and healthcare providers. A.T. gratefully acknowledges the support of the Australian Research Council for a Future Fellowship (FT200100939) and Discovery grant DP190101864. A.T. also acknowledges financial support from the North Atlantic Treaty Organization Science for Peace and Security Programme project AMOXES (#G5634). S.W. thanks the China Scholarship Council and the Australian National University for scholarship support. The authors also thank Dr. Mary Gray for proofreading/editing the manuscript.

Received:

Revised:

Published online:

References

- [1] Z. Y. Qian, S. H. Kang, V. Rajaram, C. Cassella, N. E. McGruer and M. Rinaldi, *Nat. Nanotechnol.* **2017**, *12*, 969-973.
- [2] M. Shirvanimoghaddam, K. Shirvanimoghaddam, M. M. Abolhasani, M. Farhangi, V. Z. Barsari, H. Y. Liu, M. Dohler and M. Naebe, *Ieee Access* **2019**, *7*, 94533-94556.
- [3] X. Li, C. Q. Luo, H. Ji, Y. D. Zhuang, H. L. Zhang and V. C. M. Leung, *Int. J. Commun. Syst.* **2020**, *33*, 4171.
- [4] A. Ahmed, I. Hassan, M. F. El-Kady, A. Radhi, C. K. Jeong, P. R. Selvaganapathy, J. Zu, S. Ren, Q.

This article is protected by copyright. All rights reserved.

Wang and R. B. Kaner, *Adv. Sci.* **2019**, *6*, 2925.

[5] V. A. Aksyuk, *Nat. Nanotechnol.* **2017**, *12*, 939-940.

[6] H. Askari, E. Hashemi, A. Khajepour, M. B. Khamesee and Z. L. Wang, *Nano Energy* **2018**, *53*, 1003-1019.

[7] Z. Y. Wu, T. H. Cheng and Z. L. Wang, *Sensors* **2020**, *20*, 2925.

[8] Z. L. Song, W. H. Ye, Z. Chen, Z. S. Chen, M. T. Li, W. Y. Tang, C. Wang, Z. A. Wan, S. Poddar, X. L. Wen, X. F. Pan, Y. J. Lin, Q. F. Zhou and Z. Y. Fan, *Acs Nano* **2021**, *15*, 7659-7667.

[9] E. Lee and H. Yoo, *Molecules* **2021**, *26*, 1802230.

[10] Z. Wen, Q. Q. Shen and X. H. Sun, *Nanomicro Lett.* **2017**, *9*, 45.

[11] X. L. Liu, Y. Zhao, W. J. Wang, S. X. Ma, X. J. Ning, L. Zhao and J. Zhuang, *IEEE Sens. J.* **2021**, *21*, 5628-5644.

[12] P. A. Laplante, M. Kassab, N. L. Laplante and J. M. Voas, *IEEE Intell. Syst.* **2018**, *12*, 3030-3037.

[13] Y. Kim, S. Lee, J.-G. Song, K. Y. Ko, W. J. Woo, S. W. Lee, M. Park, H. Lee, Z. Lee, H. Choi, W.-H. Kim, J. Park and H. Kim, *Adv. Funct. Mater.* **2020**, *30*, 2003360.

[14] D. Lee, H. Park, S. D. Han, S. H. Kim, W. Huh, J. Y. Lee, Y. S. Kim, M. J. Park, W. I. Park, C.-Y. Kang and C.-H. Lee, *Small* **2019**, *15*, 1804303.

[15] M. W. G. Hoffmann, L. Mayrhofer, O. Casals, L. Caccamo, F. Hernandez-Ramirez, G. Lilienkamp, W. Daum, M. Moseler, A. Waag, H. Shen and J. D. Prades, *Adv. Mater.* **2014**, *26*, 8017-8022.

[16] H. Chen, M. Zhang, R. Bo, C. Barugkin, J. Zheng, Q. Ma, S. Huang, A. W. Y. Ho-Baillie, K. R. Catchpole and A. Tricoli, *Small* **2018**, *14*, 1702571.

[17] Y. Jia, Z. Zhang, L. Xiao and R. Lv, *Nanoscale Res. Lett.* **2016**, *11*, 299.

[18] X. L. Liu, S. X. Ma, S. W. Zhu, Y. Zhao, X. J. Ning, L. Zhao and J. Zhuang, *Sens. Actuators B Chem.* **2019**, *291*, 345-353.

This article is protected by copyright. All rights reserved.

- [19] X. L. Liu, Y. Zhao, S. X. Ma, S. W. Zhu, X. J. Ning, L. Zhao and J. Zhuang, *Acs Sensors* **2019**, *4*, 3056-3065.
- [20] M. W. G. Hoffmann, O. Casals, A. E. Gad, L. Mayrhofer, C. Fabrega, L. Caccamo, F. Hernandez-Ramirez, G. Lilienkamp, W. Daum, M. Moseler, H. Shen, A. Waag and J. D. Prades, in *Euroensors 2015*, (Eds: G. Urban, J. Wollenstein and J. Kieninger) **2015**, p. 623-627.
- [21] E. Modaresinezhad and S. Darbari, *Sens. Actuators B Chem.* **2016**, *237*, 358-366.
- [22] X.-L. Liu, Y. Zhao, S.-X. Ma, S.-W. Zhu, X.-J. Ning, L. Zhao and J. Zhuang, *ACS Sensors* **2019**, *4*, 3056-3065.
- [23] M. A. Green, E. D. Dunlop, J. Hohl-Ebinger, M. Yoshita, N. Kopidakis, K. Bothe, D. Hinken, M. Rauer and X. Hao, *Prog. Photovolt.: Res. Appl.* **2022**, *30*, 687-701.
- [24] Z. Y. Li, H. H. Tan, C. Jagadish and L. Fu, *Adv. Mater. Technol.* **2018**, *3*, 1800005.
- [25] M. C. Beard, J. M. Luther and A. J. Nozik, *Nat. Nanotechnol.* **2014**, *9*, 951-954.
- [26] D. van Dam, N. J. J. van Hoof, Y. Cui, P. J. van Veldhoven, E. P. A. M. Bakkers, J. Gómez Rivas and J. E. M. Haverkort, *ACS Nano* **2016**, *10*, 11414-11419.
- [27] J. Wallentin, N. Anttu, D. Asoli, M. Huffman, I. Åberg, M. H. Magnusson, G. Siefert, P. Fuss-Kailuweit, F. Dimroth, B. Witzigmann, H. Q. Xu, L. Samuelson, K. Deppert and M. T. Borgström, *Science* **2013**, *339*, 1057-1060.
- [28] S. Wei, Z. Li, A. John, B. I. Karawdeniya, Z. Li, F. Zhang, K. Vora, H. H. Tan, C. Jagadish, K. Murugappan, A. Tricoli and L. Fu, *Adv. Funct. Mater.* **2022**, *32*, 2107596.
- [29] M. F. Schneidereit, F. Scholz, F. Huber, H. Schieferdecker, K. Thonke, N. Naskar, T. Weil and A. Pasquarelli, *Sens. Actuator B-Chem.* **2020**, *305*, 7.
- [30] J. Du, D. Liang, H. Tang and X. P. A. Gao, *Nano Lett.* **2009**, *9*, 4348-4351.
- [31] M. Bai, H. Huang, Z. Liu, T. T. Zhan, S. F. Xia, X. G. Li, N. Sibirev, A. Bouravleuv, V. G. Dubrovskii and G. Cirlin, *Appl. Surf. Sci.* **2019**, *498*, 143756.

This article is protected by copyright. All rights reserved.

- [32] Z. Y. Li, I. Yang, L. Li, Q. Gao, J. S. Chong, Z. Li, M. N. Lockrey, H. H. Tan, C. Jagadish and L. Fu, *Prog. Nat. Sci.: Mater. Int.* **2018**, *28*, 178-182.
- [33] Q. Gao, Z. Li, L. Li, K. Vora, Z. Li, A. Alabadla, F. Wang, Y. Guo, K. Peng, Y. C. Wenas, S. Mokkaapati, F. Karouta, H. H. Tan, C. Jagadish and L. Fu, *Prog. Photovolt.: Res. Appl.* **2019**, *27*, 237-244.
- [34] Q. Gao, D. Saxena, F. Wang, L. Fu, S. Mokkaapati, Y. A. Guo, L. Li, J. Wong-Leung, P. Caroff, H. H. Tan and C. Jagadish, *Nano Lett.* **2014**, *14*, 5206-5211.
- [35] Y. Kim, S. Lee, J. G. Song, K. Y. Ko, W. J. Woo, S. W. Lee, M. Park, H. Lee, Z. Lee, H. Choi, W. H. Kim, J. Park and H. Kim, *Adv. Funct. Mater.* **2020**, *30*, 2003360.
- [36] I. Yang, X. Zhang, C. L. Zheng, Q. Gao, Z. Y. Li, L. Li, M. N. Lockrey, H. Nguyen, P. Caroff, J. Etheridge, H. H. Tan, C. Jagadish, J. Wong-Leung and L. Fu, *Acs Nano* **2018**, *12*, 10374-10382.
- [37] X. Zhou, J. Y. Liu, C. Wang, P. Sun, X. L. Hu, X. W. Li, K. Shimano, N. Yamazoe and G. Y. Lu, *Sens. Actuators B Chem.* **2015**, *206*, 577-583.
- [38] T. Pham, G. Li, E. Bekyarova, M. E. Itkis and A. Mulchandani, *ACS Nano* **2019**, *13*, 3196-3205.
- [39] K. D. Wu, M. Debliquy and C. Zhang, *Chem. Eng. J.* **2022**, *444*, 136449.
- [40] H. Long, A. Harley-Trochimczyk, T. Pham, Z. R. Tang, T. L. Shi, A. Zettl, C. Carraro, M. A. Worsley and R. Maboudian, *Adv. Funct. Mater.* **2016**, *26*, 5158-5165.
- [41] J. K. Choi, I. S. Hwang, S. J. Kim, J. S. Park, S. S. Park, U. Jeong, Y. C. Kang and J. H. Lee, *Sens. Actuators B Chem.* **2010**, *150*, 191-199.
- [42] K. Y. Dong, J. K. Choi, I. S. Hwang, J. W. Lee, B. H. Kang, D. J. Ham, J. H. Lee and B. K. Ju, *Sens. Actuators B Chem.* **2011**, *157*, 154-161.
- [43] X. Z. Wang and D. Ansari, *J. En. Chem. Eng.* **2022**, *10*, 107786.
- [44] T. Pham, G. Li, E. Bekyarova, M. E. Itkis and A. Mulchandani, *ACS Nano* **2019**, *13*, 3196-3205.
- [45] D. Liu, Q. Chen, A. Chen and J. Wu, *RSC Adv.* **2019**, *9*, 23554-23559.

This article is protected by copyright. All rights reserved.

- [46] L. Liu, G. H. Li, Y. Wang, Y. Y. Wang, T. Li, T. Zhang and S. J. Qin, *Nanoscale* **2017**, *9*, 18579-18583.
- [47] T. Hamada and M. Sugiyama, *Jpn J Appl Phys* **2022**, *61*, 054002.
- [48] H. Chen, M. Zhang, X. Fu, Z. Fusco, R. Bo, B. Xing, H. T. Nguyen, C. Barugkin, J. Zheng, C. F. J. Lau, S. Huang, A. W. Y. Ho-Baillie, K. R. Catchpole and A. Tricoli, *Phys. Chem. Chem. Phys.* **2019**, *21*, 24187-24193.
- [49] M. Reddeppa, S. B. Mitta, T. Chandrakalavathi, B. G. Park, G. Murali, R. Jeyalakshmi, S. G. Kim, S. H. Park and M. D. Kim, *Curr. Appl. Phys.* **2019**, *19*, 938-945.
- [50] H. Chen, M. Zhang, B. Xing, X. Fu, R. Bo, H. K. Mulmudi, S. Huang, A. W. Y. Ho-Baillie, K. R. Catchpole and A. Tricoli, *Adv. Opt. Mater.* **2020**, *8*, 1901863.
- [51] W. C. Yi, X. Chen, Z. X. Wang, Y. C. Ding, B. C. Yang and X. B. Liu, *J. Mater.Chem. C* **2019**, *7*, 7352-7359.
- [52] V. F. Kostryukov, I. Y. Mittova and S. Ali, *Inorg. Mater.* **2020**, *56*, 66-71.
- [53] M. A. Garcia, M. Losurdo, S. D. Wolter, W. V. Lampert, J. Bonaventura, G. Bruno, C. Yi and A. S. Brown, *Sens. Lett.* **2008**, *6*, 627-634.
- [54] C. Weber, I. Sundvor and E. Figenbaum, *Atmos. Environ.* **2019**, *206*, 208-217.
- [55] P. Bera and M. Hegde, *J. Indian Inst. Sci.* **2010**, *90*, 299-325.
- [56] G. Dooly, E. Lewis, C. Fitzpatrick and P. Chambers, *IEEE Sens. J.* **2007**, *7*, 685-691.
- [57] S. Karthikeyan, E. M. Thomson, P. Kumarathasan, J. Guénette, D. Rosenblatt, T. Chan, G. Rideout and R. Vincent, *Toxicol. Sci.* **2013**, *135*, 437-450

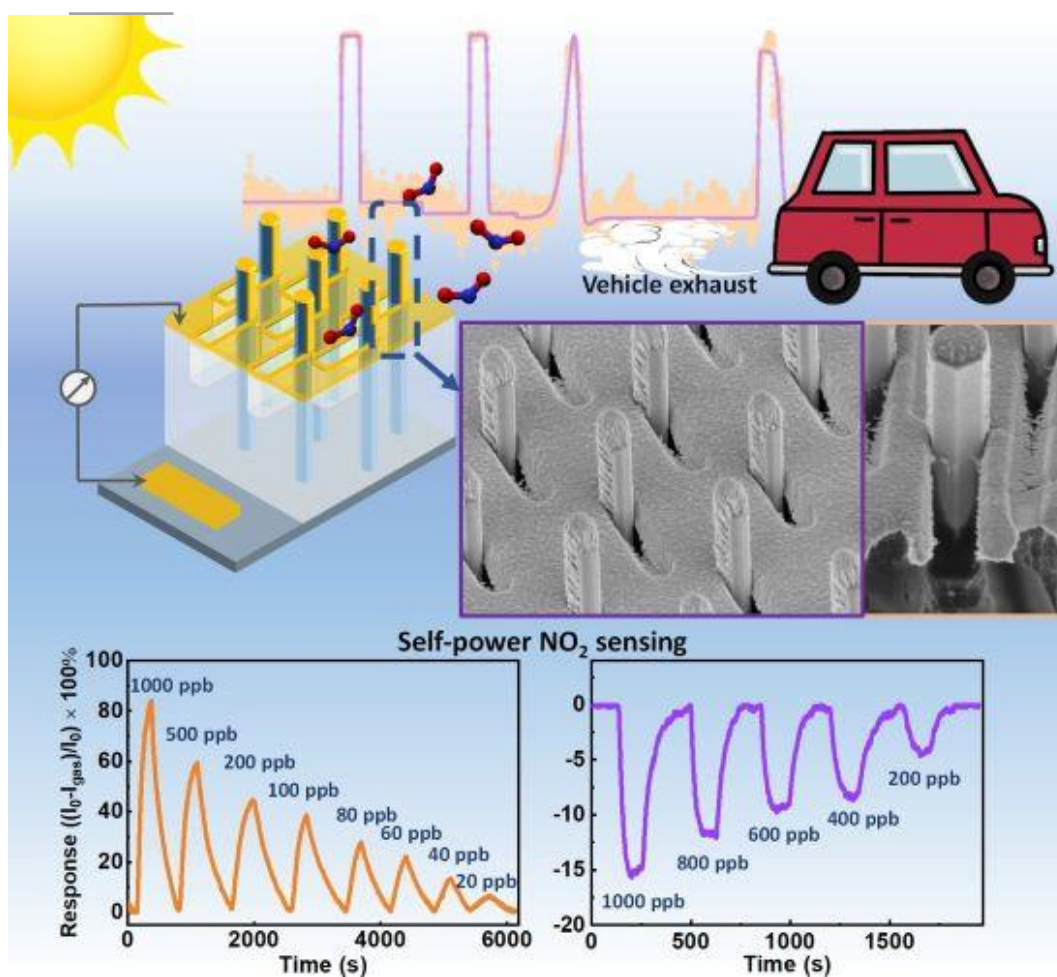
The table of contents

This article is protected by copyright. All rights reserved.

An innovative self-powered room-temperature nitrogen dioxide (NO_2) sensor is presented based on indium phosphide homojunction nanowire array. The proof-to-concept sensor structure has been demonstrated with high sensitivity, stability and selectivity. It is integrated to USB interface for on-field vehicle exhaust measurement. This work promises a new family of self-powered sensor made of III-V compound semiconductor nanostructures, for future mega-scale Internet-of-Things systems.

S. Wei, Z. Li, K. Murugappan, Z. Y. Li, F. Zhang, M. Lysevych, H. H. Tan, C. Jagadish, A. Tricoli, L. Fu

Self-Powered Portable Nanowire Array Gas Sensor for Dynamic NO_2 monitoring at room temperature



This article is protected by copyright. All rights reserved.